

MECHANISMS OF ACTIVE AERODYNAMIC LOAD REDUCTION ON A ROTORCRAFT FUSELAGE WITH ROTOR EFFECTS

Norman W. Schaeffler
Senior Research Scientist

Brian G. Allan
Senior Research Scientist

Luther N. Jenkins
Senior Research Scientist

Chung-Sheng Yao
Senior Research Scientist

Flow Physics and Control Branch
NASA Langley Research Center
Hampton, Virginia, USA

Scott M. Bartram
Optics Specialist
Advanced Sensing and Optical Measurement Branch
NASA Langley Research Center
Hampton, Virginia, USA

W. Derry Mace
Instrumentation Specialist
Sierra-Lobo
Hampton, Virginia, USA

Oliver D. Wong
Senior Research Scientist
U.S. Army Aviation Development Directorate - AFDD(AMRDEC)
Joint Research Program Office
NASA Langley Research Center
Hampton, Virginia, USA

Philip E. Tanner
Research Scientist

The reduction of the aerodynamic load that acts on a generic rotorcraft fuselage by the application of active flow control was investigated in a wind tunnel test conducted on an approximately 1/3-scale powered rotorcraft model simulating forward flight. The aerodynamic mechanisms that make these reductions, in both the drag and the download, possible were examined in detail through the use of the measured surface pressure distribution on the fuselage, velocity field measurements made in the wake directly behind the ramp of the fuselage and computational simulations. The fuselage tested was the ROBIN-mod7, which was equipped with a series of eight slots located on the ramp section through which flow control excitation was introduced. These slots were arranged in a U-shaped pattern located slightly downstream of the baseline separation line and parallel to it. The flow control excitation took the form of either synthetic jets, also known as zero-net-mass-flux blowing, and steady blowing. The same set of slots were used for both types of excitation. The differences between the two excitation types and between flow control excitation from different combinations of slots were examined. The flow control is shown to alter the size of the wake and its trajectory relative to the ramp and the tailboom and it is these changes to the wake that result in a reduction in the aerodynamic load.

Nomenclature

A_{CS} Fuselage cross-sectional area (maximum), ft^2
 A_j Jet slot exit area, ft^2
 C_D Fuselage drag coefficient, $D/(q_\infty A_{CS})$
 C_L Fuselage lift coefficient, $L/(q_\infty A_{CS})$
 C_p Pressure coefficient, $(p - p_s)/q_\infty$
 C_T Rotor thrust coefficient, $T/\rho_\infty \pi R^2 (\Omega R)^2$
 C_μ Momentum coefficient

D Fuselage drag force in the wind axis, lbs
 F^+ Reduced frequency, fW/U_∞
 f Excitation frequency, Hz
 H Fuselage height (maximum), $inches$
 L Fuselage lift force in the wind axis, lbs
 M Mach number
 \dot{m} Mass flow rate, lb_m/s
 q_∞ Freestream dynamic pressure, $\frac{1}{2}\rho_\infty U_\infty^2$, psi
 Re Reynolds number, $U_\infty(2R_F)/\nu$
 R Rotor radius, $inches$
 R_F Reference rotor radius, $inches$
 T Rotor thrust, lbs
 U_∞ Freestream velocity, ft/s
 V_j Jet exit velocity, either peak or bulk, ft/s

Presented at the American Helicopter Society Technical Meeting on Aeromechanics Design for Vertical Lift, San Francisco, CA, January 20-22, 2016. This is a work of the U.S. Government and is not subject to copyright protection in the United States of America.

W	Fuselage width (maximum), <i>inches</i>
X/R_F	Normalized streamwise coordinate
Y/R_F	Normalized spanwise coordinate
Z/R_F	Normalized vertical coordinate
α	Fuselage angle of attack, <i>degrees</i>
ΔC_D	Change in the drag coefficient as a percentage of the baseline
ΔC_L	Change in the lift coefficient as a percentage of the baseline
μ	Rotor advance ratio
ν	kinematic viscosity, ft^2/s
Ψ	rotor azimuth angle - Blade 1, degrees
ρ	Density, $slugs/ft^3$
σ	Thrust-weighted rotor solidity

Introduction

For a large number of rotorcraft, the design for the fuselage is guided by maximizing the mission utility of the vehicle rather than its aerodynamic efficiency. This can result in a flowfield around the fuselage that tends to resemble the flowfield around a bluff-body, with the flow around the aft end of the fuselage being dominated by massive flow separation. This leads not only to a large amount of pressure drag acting on the fuselage, but also to a higher level of rotor-induced download, or negative lift. It has been noted that the cruise drag of a rotorcraft is typically an order of magnitude higher than the cruise drag of a fixed-wing aircraft of the same gross weight (Ref. 1) and also that, for rotorcraft operating at high forward speed, half of the power delivered by the main rotor is used to overcome the aerodynamic forces, drag and download, acting on the fuselage (Ref. 2). If the application of active flow control (AFC) could be used to deliver back aerodynamic efficiency to an otherwise aerodynamically inefficient fuselage design, the range, speed, and/or fuel efficiency of the vehicle could be increased and its mission utility would not only be preserved, but enhanced. The work of Martin et al. (Ref. 3) and Ben-Hamou et al. (Ref. 4) has demonstrated that active flow control can be applied to achieve a reduction in drag on an isolated fuselage. This directly led to further work in applying AFC to the problem of drag reduction on an isolated fuselage, specifically the work of Schaeffler et al. (Ref. 5), Woo et al. (Ref. 6), Coleman and Thomas (Ref. 7), and Le Pape et al. (Ref. 8). Once the research transitioned from an isolated fuselage to a fuselage in the presence of a rotor, attention also needed to be paid to the download, or negative lift, developed by the fuselage, in addition to the drag. This is because care must be taken to ensure that any flow control strategies that are identified to reduce the fuselage drag, do not have an adverse effect on the download.

One of the key differences between rotary-wing aerodynamics and fixed-wing aerodynamics can be illustrated by a simple force balance. For a fixed-wing aircraft in steady flight, lift balances weight and thrust balances drag. If, through the application of active flow control, the drag acting on the fixed-wing aircraft, in steady level flight, was reduced, the thrust required would be correspondingly reduced and the lift and

weight would be unaffected and remain in balance. For a rotorcraft, the picture is slightly more complicated. The thrust developed by the rotor disk, again in steady level flight, is used both to balance the weight and any negative lift that the fuselage generates and also to balance the drag. This raises a question when it comes to judging the effectiveness of any drag reduction strategy: What is the impact of the drag reduction on the download experienced by the fuselage under the influence of a rotor? Since the rotor is responsible for providing both the lifting force for the rotorcraft and the propulsive force for forward flight, any benefit from a reduction in drag could be offset by an increase in download, effectively limiting any benefit from applying the flow control. Thus, it would be preferred that any flow control strategies identified to reduce the fuselage drag also reduce the download acting on the fuselage.

The current research effort is the final wind tunnel test of a study that was undertaken to examine the application of active flow control for drag and download reduction on a generic, nonproprietary, fuselage. The study reported here was conducted under the NASA Rotary Wing (RW) Project, now the NASA Revolutionary Vertical Lift Technology (RVLT) Project. It has been, since its inception, an integrated experimental and computational research effort that started with the creation of a new fuselage geometry followed by small-scale wind tunnel investigations of the baseline characteristics of the isolated fuselage and corresponding simulations. The integrated experimental and computational approach of this work allowed the baseline aerodynamic characteristics to be documented and validated simultaneously (Ref. 5). Out of this effort, and a related collaboration between NASA and ONERA, a flow control strategy was identified computationally for the isolated fuselage at 0° angle of attack. This flow control strategy was then applied computationally to the more relevant environment of a fuselage at a negative angle of attack and rotor operating at high advance ratio (Ref. 9). These conditions are typical of rotorcraft operating at high speed and are the conditions under which the drag and download reductions are desired. The computational effort allowed for the study of the effect of the rotor and its wake on the fuselage drag and download. It provided a mechanism for evaluating the effectiveness of active flow control in reducing the drag and download forces and for how different flow control actuator parameters, such as slot size, frequency, and peak jet velocity, affected the level of load reduction. Ultimately, the combined knowledge gained from the computations and the earlier experimental work enabled the design of the slot layout and flow control strategy that was tested experimentally in the current research effort. The final wind tunnel entry had three distinct phases, each of which utilized a different ramp section on the fuselage. The first phase of the entry was devoted to the application of pressure-sensitive paint (PSP) to the upper surface of one of the rotor blades and utilized a clean, unmodified, ramp section. Interested readers can find a description of the PSP experimental work in Watkins et al. (Ref. 10). The second phase of the entry was the one that is reported here, and also in Schaeffler et al. (Ref. 11), and featured a ramp

section equipped with eleven slots through which flow control excitation could be delivered. Finally, the third phase of the entry was also an active flow control experiment that utilized a ramp equipped with fluidic actuators for load alleviation and the results from this phase are reported in Martin et al. (Ref. 12). Additionally, a comprehensive report of both of the active flow control phases of the entry can be found in Ballard et al. (Ref. 13).

Experimental Facility and Model

The current research effort was conducted in the NASA Langley 14- by 22-Foot Subsonic Tunnel (14x22). The 14x22 is a closed-circuit, single-return, atmospheric wind tunnel with a reconfigurable test section. The test section can be operated in either an open or closed configuration. For the work presented here, the tunnel was operated in the closed configuration in which the test section has the dimensions of 14.5 ft high, 21.75 ft wide, and 50 ft long and can achieve a maximum speed of 348 ft/s with a dynamic pressure of 144 psf. The airflow in the test section is produced by a 40 ft diameter, 9-bladed fan driven by a 12,000 hp main drive. Additional information about the 14x22 can be found in Gentry et al. (Ref. 14).

The model utilized in this research effort was comprised of the General Rotor Model System (GRMS) and the ROBIN-mod7 (ROtor Body INteraction) fuselage. The GRMS is a rotor drive system that is powered by two, 75 hp, water-cooled electric motors that drive a 5.47:1 transmission. The rotor system driven by the GRMS consisted of a fully-articulated rotor hub and a set of four rotor blades, which utilize Government RC-series airfoils. The rotor system had a diameter of 11.08 feet and the cuff of one of the rotor blades was instrumented to measure blade pitch, lead-lag, and flapping angles. Detailed properties for the rotor system can be found in Wong et al. (Ref. 15).

The GRMS is equipped with two independent six-component strain gage force and moment balances, one for measuring the loads acting on the fuselage and one for measuring the loads acting on the rotor. There are accelerometers mounted within the GRMS to monitor the operational loads acting on the complete system during testing. There is also a rotor shaft encoder, which provided both 1/Rev and 1024/Rev timing signals. These timing signals were used for synchronizing the data acquisition and the timing of the flow control to the azimuthal position of the rotor. The rotor system was operated at a rotational speed of 1150 RPM, which resulted in a hover rotor tip Mach number of 0.58. The rotor system was designed with a nominal shaft tilt angle of -3° relative to the fuselage. Additional details regarding the GRMS can be found in Wilson (Ref. 16).

The ROBIN-mod7 fuselage was developed for the initial small-scale testing that preceded the current research effort (Ref. 5) and is a variation of the ROBIN fuselage geometry, which was developed at NASA Langley in the 1970s. The original ROBIN was developed to be representative of

a generic helicopter and also to be analytically defined, allowing it to be easily reproduced for calculations (Ref. 17). The original ROBIN fuselage has been utilized in several other wind tunnel investigations (Refs. 18, 19) and is widely used in the rotorcraft CFD community (Refs. 20, 21). To arrive at the ROBIN-mod7 fuselage, the standard coefficients that define the ROBIN fuselage were modified to create a new fuselage geometry that has a rectangular, as opposed to square, cross-section, a well-defined ramp section, and a high tailboom. The fuselage calculation procedure and the modified coefficients for the ROBIN-mod7 are discussed fully in Schaeffler et al. (Ref. 5). This new fuselage is representative of a generic helicopter fuselage within the light to medium range of civil configurations with a large aft loading cargo section, typical of a commercial rotorcraft that encounters a large fuselage drag at high-speed. Following the ROBIN convention, the fuselage length is scaled to a reference rotor radius, R_F , which results in a non-dimensional fuselage length of $2R_F$. Since its introduction, the ROBIN-mod7 fuselage has been adopted by other researchers within the rotorcraft community (Refs. 22–24), particularly those exploring the application of active flow control on rotorcraft fuselages (Refs. 6, 7, 25). For the ROBIN-mod7 fuselage tested in 14x22, the size is based upon a reference rotor radius of 61.9655 inches, with a total fuselage length of 123.931 inches ($X/R_F = 2.0$). In reference to a medium civil rotorcraft, it can be considered an approximately 1/3-scale model. The fuselage geometry and dimensions can be seen in Fig. 1. It is worth noting that the rotor system utilized in the current work is oversized for the fuselage by about 7% and, due to the sting mounting utilized in the current research effort, the tail cap, which closes off the tailboom, is not used. This shortens the overall length of the fuselage to 105 inches ($X/R_F = 1.694$).

For this research effort, the ROBIN-mod7 fuselage and the GRMS were mounted to a sting adapter and long cannon, which, in turn, was mounted to the mast of one of the 14x22 facility model carts installed in the aft bay of 14x22. Due to the length of the long cannon, GRMS and the ROBIN-mod7 fuselage end up positioned over a filler cart, which was installed in the front bay of 14x22. The mast on the aft cart provides both pitch and elevation control, enabling the model to be positioned at a range of fuselage angles of attack while maintaining a constant height of the rotor hub, nominally 87 inches, in the test section. The model was only tested at 0° yaw. The complete model installation in the 14x22 can be seen in Fig. 1(e).

Eight of the flow control slots were laid out symmetrically with respect to the fuselage vertical centerline and as close to a continuous U-shape, that the constraints of packaging actuators on the inside of the fuselage shell would allow. This arrangement can be seen schematically in Fig. 1. On the fuselage, this U-shaped group of slots is aligned 23° from the vertical, which is the same orientation as, and slightly downstream of, the flow separation line of the baseline configuration. The slot height was 0.020 inches and the slots were oriented at a 25° angle to the local surface. Each of the slots was assigned a number. When looking upstream from behind

the model, which is the view as shown in Fig. 1(f), slot 1 was the uppermost slot on the left, or port, side. Slots 2 and 3 were along the port side and slot 4 was the slot along the bottom of the fuselage and the slot closest to the fuselage vertical centerline on the port side. This pattern continued on the starboard side of the fuselage with slot 5 being on the bottom and closest to the centerline, slots 6 and 7 being on the starboard side, and slot 8 being the uppermost slot on the starboard side. Three additional slots were located upstream of the primary eight slots, slots 9, 10, and 11, and these are visible in Fig. 1(f). Flow control cases involving these slots will not be discussed here.

During the course of the experiment, each of the slots were connected to either a pressurized plenum that delivered a steady blowing excitation through the slot or to a synthetic jet actuator that delivered an oscillatory suction-blowing excitation through the slot, also known as zero-net-mass-flux (ZNMF) blowing. Each of the eleven synthetic jet actuators had its own drive signal and amplifier to allow the phasing and amplitude of the excitation to be independently controlled on a slot-by-slot basis. The 1/Rev and 1024/Rev timing signals from the GRMS were utilized to synchronize the phasing of the synthetic jet actuators and the data acquisition with respect to the rotor. When configured for the synthetic jet actuators, the temperature of each of the drivers and the cavity pressure of each of the cavities were monitored and recorded. When configured for steady blowing, the cavity pressure within each of the pressurized plenums and the total pressure at the inlet of each plenum was measured by an Electronically Scanned Pressure (ESP) module mounted within the fuselage. Only four control valves were used in the steady blowing portion of the test. Each valve supplied air to two plenums enabling the slots to be activated in pairs symmetric with respect to the fuselage centerline.

For both synthetic jet excitation and steady blowing, different configurations of active and non-active slots were tested. Two of these configurations were given names. For the first configuration, referred to as the U-configuration, all eight of the slots were active. The second configuration, referred to as Ux45-configuration, modifies the U-configuration such that the two center slots, slots 4 and 5, were not active.

The definition of the momentum coefficient, C_μ , was different for each of the flow control excitations. For the synthetic jet portion of this effort, the momentum coefficient was defined based upon the peak jet velocity at the jet exit and was computed using Eq. 1:

$$C_\mu = \frac{\sum(\rho_j V_j^2 A_j)}{q A_{CS}}. \quad (1)$$

Due to the packaging of the actuators within the fuselage shell and the geometry of the ramp region, the slot lengths for each of the slots were not exactly the same. However, the slot lengths were symmetric with respect to the centerline of the fuselage. The actual slot lengths were used in calculating the jet areas, along with the slot height of 0.020 inches. The density, ρ_j , was assumed to be the same as the density of the air in the test section.

For the steady blowing portion of this effort, the momentum coefficient, C_μ , was defined based upon the total mass flow, as measured by an inline flowmeter upstream of the four valves that control which of the slot pairs are active. The jet velocity was computed based on the mass flow and the slot area and thus, represents the bulk velocity of the jet. The total and cavity pressures measured in the plenum of each slot were used during the experiment to balance the mass flow. The momentum coefficient was computed as follows:

$$C_\mu = \frac{\dot{m} V_j}{q A_{CS}}. \quad (2)$$

Throughout, C_μ can alternatively be presented as a pure number or a percentage, as in $C_\mu = 0.025$ or $C_\mu = 2.50\%$.

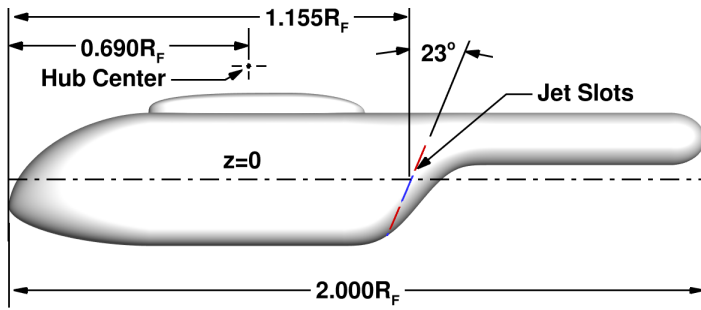
Stereo Large Field-of-View PIV System

To investigate and document the effect of different active flow control configurations on the fuselage wake, off-body measurements were made using a Large Field-of-View PIV System (LFPIV). LFPIV has been used in the 14x22 for several years and has proven to be a valid and efficient tool to document wake flows for both fixed-wing and rotary-wing configurations.

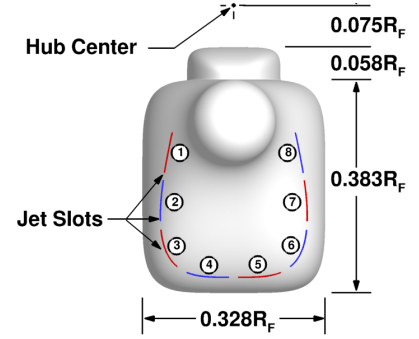
The PIV system was composed of two 1.5 Joule Nd-YAG lasers and two, 11 Megapixel, cameras equipped with 210 mm focal length lenses. Since the test section was closed for this test (i.e., walls and ceiling down), optical access was limited to windows in the tunnel sidewalls. On the south side of the tunnel, the laser beam passed through a set of sheet-forming optics to create a lightsheet that was then projected through one of the sidewall windows to the measurement plane downstream of the fuselage ramp. The lightsheet was inclined 10 degrees relative to vertical in order to make the measurement plane nearly parallel to the ramp when the model was set at negative angles of incidence as depicted in Fig. 2, which also shows the relationship between the measurement plane and the width of the fuselage. At the nominal test angles, the measurement plane intersected the tailboom at $X/R_F = 1.31$.

For this test, a stereoscopic PIV configuration was used to measure three components of velocity. Cameras were positioned in window cavities on opposite sides of the tunnel, which placed one camera in back scatter and one camera in forward scatter. The working distance for each camera was nearly 4.2 meters (13.78 feet). This distance, coupled with the camera angle and sensor size resulted in a field of view of approximately 838 mm by 481 mm (width x height). Based on the camera sensor size, 4008 pixels by 2680 pixels, the magnification was estimated to be 0.216 mm/pixel.

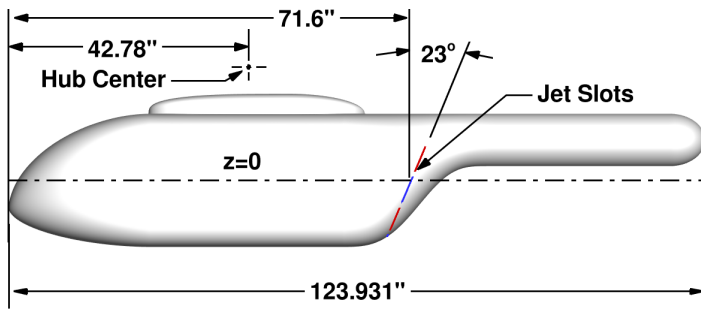
The flow was seeded using a mineral oil based mixture and a commercial fog machine, which produced polydispersed particles ranging in diameter from 0.25 microns to 1.5 microns. The particles were injected into the flow at the rear of the test section near the diffuser and distributed uniformly by the fan before entering the test section.



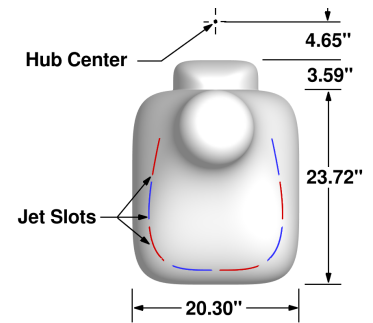
(a) Side view - non-dimensional



(b) Rear view - non-dimensional



(c) Side view - 14x22 dimensions



(d) Rear view - 14x22 dimensions



(e) The ROBIN-mod7 model mounted on the GRMS and the long cannon sting.



(f) Rear view of the model highlighting the actuator layout.

Fig. 1. The ROBIN-mod7 fuselage: Dimensions and as a model installed in the 14x22 Subsonic Tunnel.

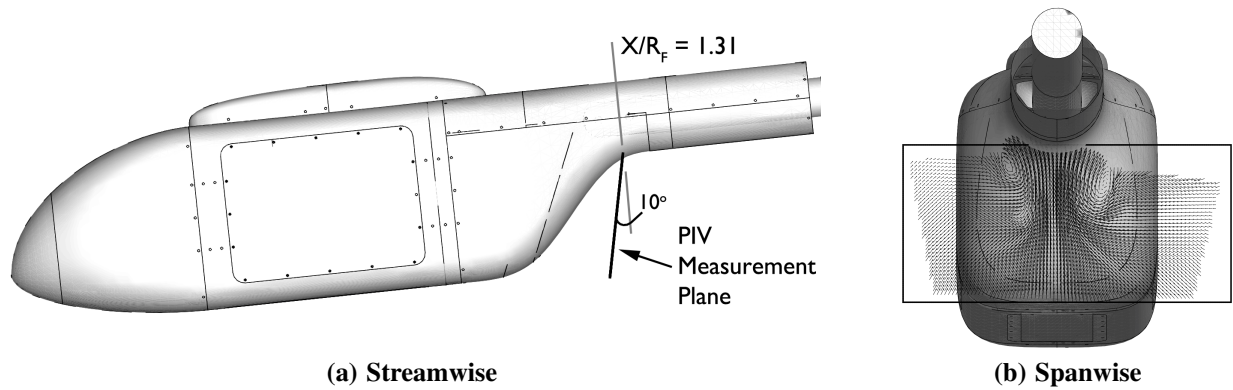


Fig. 2. The ROBIN-mod7 model as a schematic showing the location and orientation of the PIV measurement plane in the streamwise and the spanwise directions. The model is illustrated at an angle of attack of -6° .

For each active flow control configuration, a minimum of 100 images were acquired synchronized with a pre-set azimuth angle of the rotor. These images were then processed using an interrogation area of 64 pixels by 64 pixels with an overlap of 50%. This corresponds to a spatial resolution of 13.8 mm by 13.8 mm. The uncertainty in the averaged velocities is estimated to be 1 m/s.

Forward Flight at an Advance Ratio of 0.25

As stated in the *Introduction*, the current research effort has been carried out since its inception as a combined experimental and computational effort. In addition to the computational investigations conducted before the mid-scale testing began, which are summarized by Allan et al. (Ref. 9), a series of computational fluid dynamics (CFD) simulations were conducted after the completion of the experimental efforts. These were conducted to simulate specific cases as close to the experimental conditions as possible and to provide an assessment of the performance of two turbulence models. The results were compared to the experimental data and also used to yield additional insight into the mechanisms involved in the observed drag and download reductions. All of these simulations were carried out at an advance ratio of 0.25, a fuselage angle of attack of -6° and a thrust condition of $C_T/\sigma = 0.075$. The steady blowing excitation proved more robust than the synthetic jet excitation at this advance ratio, so only steady blowing cases were selected for simulation.

The numerical simulations were conducted using OVERFLOW solving the compressible Reynolds-averaged Navier-Stokes (RANS) equations. The Spalart Allmaras (SA) (Ref. 26) and Shear Stress Transport (SST) (Ref. 27) turbulence models were used for the numerical simulations with a Rotational/Curvature Correction (RCC) model, as implemented in OVERFLOW (Ref. 28). The time-accurate rotor/fuselage simulations used a dual-time stepping method with time steps equivalent to 0.125° rotor revolutions with 40 sub iterations per time step. The rotor dynamics were simulated using a loose coupling between OVERFLOW and the comprehensive rotorcraft code, CAMRAD-II (Refs. 29, 30).

The rotor blades are modeled as nonelastic blades with flapping and lead/lag motions. This loose coupling was performed every half revolution of the rotor. A complete description and analysis of all of the post-test CFD can be found in Allan et al. (Ref. 31).

A key observation from the computational analysis involves the trajectory of the wake for both the baseline and control cases and the origin of the additional aerodynamic loads acting on the fuselage in the presence of the rotor. Iso-surface contours of vorticity magnitude are presented in Fig. 3 from the OVERFLOW simulations using the SA turbulence model. These iso-surface contours are for a single vorticity magnitude value and are shaded by the local pressure coefficient. The rotor azimuth angle of the data presented here is 0° , corresponding to a rotor blade directly over the tail, or equivalently the nose. For the baseline case, Fig. 3(a), the vorticity iso-surfaces indicate that as the flow rounds the shoulder of the ramp it remains attached for a short distance up the ramp and then separates. While the flow is separated, it still follows the general shape of the ramp until it is turned by the tailboom. This description is reinforced by looking at the measured centerline surface pressure distribution, which is presented in Fig. 4. Here the centerline pressures for the baseline case indicate that the flow remains attached as it rounds the ramp shoulder, separates shortly thereafter, and then follows the general shape of the ramp rather than remaining in a more streamwise direction. For Fig. 4, and the other measured centerline surface pressure figures to follow, the symbols on the solid lines corresponds to pressure taps on the fuselage centerline. The dashed line is included to give an indication of the strength of the suction peak at the ramp shoulder and the single symbol on each of these lines is an averaged value from two pressure taps symmetrically offset from the centerline in the spanwise direction ($Y/R_F = \pm 0.051$).

For both of the steady blowing control cases, Figs. 3(b) and 3(c), the vorticity iso-surfaces indicate that the wake moves in more of a streamwise direction than does the baseline case. The wake does not follow the geometry of the ramp and it stays further away from the tailboom. This is also seen in centerline surface pressures in Fig. 4. Both of the control

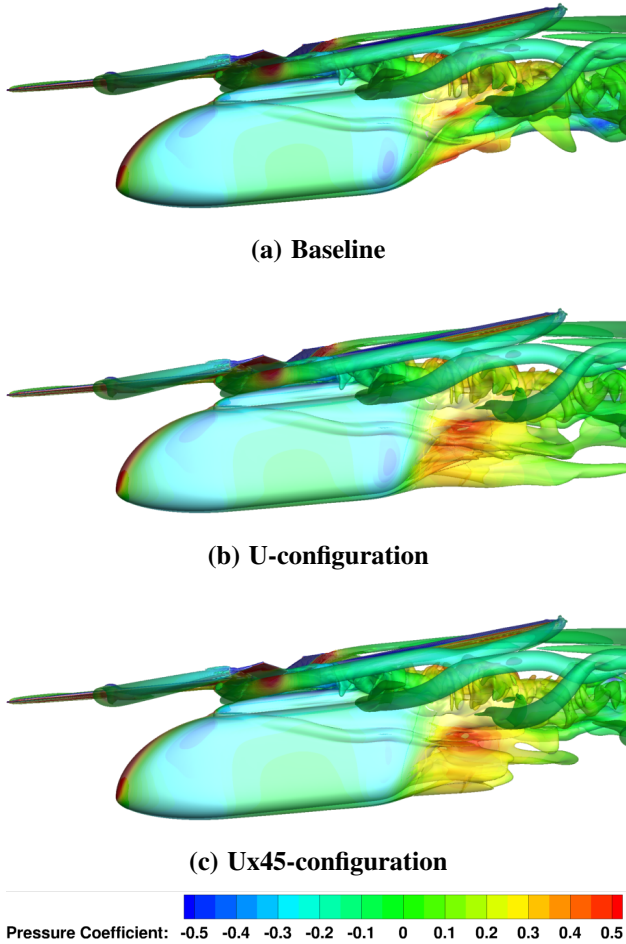


Fig. 3. Vorticity magnitude iso-surface contours shaded by C_p for the baseline, U-, and Ux45-configurations from the CFD simulations using the SA turbulence model, at a rotor azimuth angle of 0° . AFC = Steady Blowing at $VR = 2.6$, $\mu = 0.25$, $C_T/\sigma = 0.075$, and $\alpha = -6^\circ$

cases have a reduced suction peak indicating an earlier separation than the baseline case with the Ux45-configuration showing less of a tendency to follow the shape of the ramp. For these control cases, as throughout, when comparing the U-configuration to the Ux45-configuration, the ratio of the jet velocity to the freestream velocity, the velocity ratio VR , is held the same. For the cases here, the $VR = 2.6$ corresponds to a $C_\mu = 2.07\%$ for the U-configuration and $C_\mu = 1.67\%$ for the Ux45-configuration, experimentally.

In Fig. 5(a), the experimentally measured surface pressure on the upper portion of the nose of the fuselage ($X/R_F = 0.200, Y/R_F = 0.016, Z/R_F = 0.145$) versus the rotor azimuth angle is presented. The high values of pressure as the rotor blades pass over the nose are clearly seen and correspond to the high pressure level seen on the nose in Fig. 3, which is shaded red. These high pressure loadings as the blade passes over the nose generate forces that push the nose down, increasing the download, and push the nose aft, increasing the drag. These blade passage events correspond to the peaks in the drag and the maximum negative values for the lift seen in

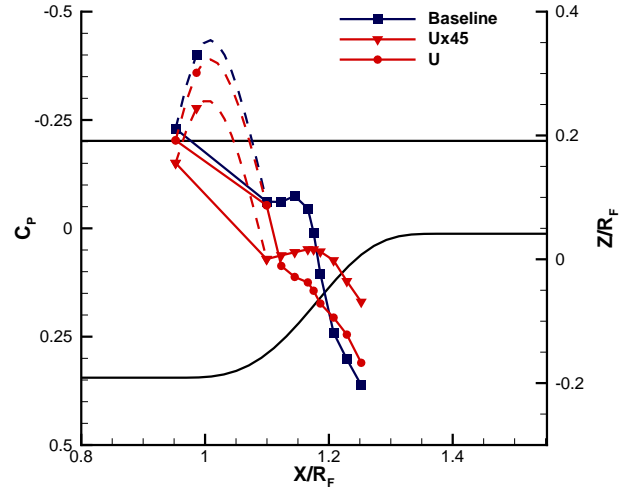


Fig. 4. Measured surface pressure distribution over the centerline of fuselage ramp section. AFC = Steady Blowing at $C_\mu = 2.07\%$ for the U-configuration and $C_\mu = 1.67\%$ for the Ux45-configuration ($VR = 2.6$ for both), $\mu = 0.250$, $C_T/\sigma = 0.075$, $\alpha = -6^\circ$. The black lines are the fuselage geometry.

the predicted aerodynamic loads, Fig. 5(b). They are the origin of the additional aerodynamic loading that the presence of the rotor generates on the fuselage.

Building upon the insight gained from the computational results, consider the velocity field on a plane immediately downstream of the fuselage ramp as measured by the large-field-of-view stereo PIV system. In Fig. 6, a representative example of the complete measured velocity field is presented from a viewpoint looking upstream at the ramp section. It is presented in horizontal and vertical coordinates as measured within the PIV measurement plane and nondimensionalized by the reference rotor radius for the fuselage. The stereo PIV measurements result in a vector field wider than the width of the fuselage, which is ± 0.164 in the same coordinates. The black semi-circle represents the size and location of the tailboom, relative to the measurement plane. The vectors plotted are the in-plane components relative to the measurement plane. There are a maximum of 114 vectors horizontally and a maximum of 52 vectors vertically. In the nondimensionalized coordinates, the vector spacing is 0.00877.

In order to make the vector field easier to visualize, from this point forward, a convention will be adopted where every other vector horizontally is skipped and only every third vector vertically is presented. This allows the vectors to be displayed with a longer length, thus allowing the overall in-plane pattern of the flow field to be visualized. The out-of-plane component of the velocity will be represented by color contours. The contours from the part of the plane where measurements were not taken are suppressed by not showing contours below a value of $U_{PIV}/U_\infty = 0.07$. An additional convention was adopted that the width of the wake will be indicated by only presenting contours of the out-of-plane velocity, which are less than 0.9 times the freestream velocity

($U_{PIV}/U_\infty \leq 0.90$).

Following these conventions, the velocity fields for the baseline, U- and Ux45-configurations are presented in Fig. 7. The acquisition of the PIV data was synchronized with the rotor through the use of the 1/Rev pulse generated by GRMS when the leading edge of blade 1 passes over the tail and this position is a rotor azimuth angle of 0° . The PIV data presented here is for two different rotor azimuth angles, 23° , which will be the standard angle unless otherwise noted, and 60° . The baseline, Figs. 7(a) and 7(c), does show some slight changes as the blade 1 moves further away from the measurement plane, however the general features are the same. The width of the wake is roughly the width of the fuselage. There are two regions of low out-of-plane velocity on either side of the tailboom. In between them, there is a region of large vertical velocity that is roughly as wide as the tailboom. As was seen in Fig. 3(a), since the flow behind the ramp in the baseline configuration is following the shape of the ramp even though the flow is separated, the flow will exhibit a large vertical velocity component when it encounters the PIV measurement plane. It has been noted by Martin et al. (Ref. 12), that cases where a region of large vertical component of velocity exist directly under the tailboom are also cases that exhibit a large amount of download acting on the fuselage. Here it can be seen that it is the trajectory of the wake that causes both the region of large vertical component of velocity and the surface pressure distribution that generates the download.

For the U-configuration, Fig. 7(b), the low out-of-plane velocity region on the port side has been eliminated and the one on the starboard side has been moved a significant distance away from the tailboom. Also, the vertical velocity in the area directly under the tailboom has been reduced. As was seen in Figs. 3(b) and 3(c), when the flow over the ramp is being controlled in either the U-configuration, or the Ux45-configuration, the result is the wake is moving in more of a streamwise direction and as it encounters the PIV measurement plane, the observed vertical velocity component will be small. In fact for the Ux45-configuration, Fig. 7(d), that region of large vertical velocity has been replaced by a large region of low out-of-plane velocity directly under the tailboom. It is this region that generates the characteristic shape of the surface pressure distribution for the Ux45-configuration seen in Fig. 4 and a corresponding reduction in download. For the Ux45-configuration, the experimental aerodynamic load reduction was a 53.8% download reduction with a 24.4% drag reduction. For the U-configuration, the experimental aerodynamic load reduction was a 39.2% download reduction with a 25.2% drag reduction.

“Building The U”

In Fig. 8, the change in drag and lift coefficients as a function of the momentum coefficient, C_μ , is presented. Typically, data presented like this would be used to indicate an increase in the level of excitation, e.g., increasing the jet velocity out of a single slot. Here, however, the jet velocity is remaining approximately constant and it is the number of active slots that are

changing. For each of the C_μ values plotted, an additional pair of slots is activated. This is being done in sequence starting with the upper pair, slots 1 and 8, and continuing until all the slot pairs are active. Pair 1 (P1) would be slots 1 and 8, pair 2 (P2) would be slots 2 and 7, pair 3 would be slots 3 and 6, and pair 4 would be slots 4 and 5. The second to the last C_μ value plotted would correspond to the Ux45-configuration and the final value plotted would correspond to the U-configuration.

The performance levels for drag and download reduction that are achieved by just the P1-configuration is quite impressive. The first quarter of the C_μ invested in the load reductions achieved half of the overall reduction, a ΔC_D of -12.6% for just the P1-configuration versus -25.2% for the U-configuration and a ΔC_L of -27.0% for just the P1-configuration versus -53.8% for the Ux45-configuration, the configuration which produces the maximum download change. Adding the second set of slots, so that P1 and P2 are active, brings the performance very close to the maximum values achieved. An additional 5% drag reduction can be had if the last two sets of slots are activated, resulting in the U-configuration, but it comes at a cost of increasing the C_μ required for the first 20% reduction by 53%. Additionally, very little change in download reduction is achieved by adding in the third pair of slots, which is the Ux45-configuration, and there is the same penalty for the download reduction with the U-configuration that we have seen before. The centerline surface pressure distribution on the ramp section for each of these cases is presented in Fig. 9.

In Fig. 10, the baseline, P1-configuration, P1+P2-configuration, and the U-configuration velocity fields are presented. The rotor azimuth angle for the acquisition of all of these was 23° . For the baseline case, Fig. 10(a), there are two regions of low out-of-plane velocity below and on either side of the tailboom with an area of high upwash, or high vertical velocity, between them directed towards the lower surface of the tailboom. As noted earlier, this indicates that, while the flow in the baseline case is separated, the flow is still following the general shape of the ramp such that the flow has a high vertical velocity component when it encounters the PIV measurement plane. Evidence of this flow pattern can be seen in the CFD simulation results presented in Fig. 3 for the baseline case. The width of the wake is approximately the width of the fuselage, the fuselage width is $\pm Y/R_F = 0.164$.

In Fig. 10(b), the effect on the velocity field in the wake from steady blowing in the P1-configuration can be seen. There is still a region of large vertical velocity, but its magnitude close to the tailboom is greatly reduced. It can also be seen that the wake is contracted by a small amount. There is a much larger low-speed region to the right hand side of the tailboom centerline. When the second slot pair is brought on-line, this low-speed area grows in size, as seen in Fig. 10(c), and the area of high vertical velocity component directly under the tailboom has been removed. This indicates that the flow over the ramp and into the wake is no longer following the general shape of the ramp, but is instead separating from the ramp and moving in a more streamwise fashion, as we saw in the CFD iso-surfaces presented in Fig. 3 for the control cases.

Within the low speed region, the flow is reversed, as shown in Fig. 11, but the magnitude of the out-of-plane velocity is very small, with the measurements indicating a maximum reversed flow velocity of $0.7\% U_\infty$. If the last two pairs of slots are brought on-line, resulting in the U-configuration, and shown in Fig. 10(d), some of the large vertical velocity directly under the tailboom returns and the low-speed region is greatly reduced in size and moves further away from the tailboom than in the previous cases. The U-configuration presented here has the largest drag reduction of this set and the smallest area of reversed flow, but produces less download reduction than the Ux45-configuration. This is due to the wake having less of a streamwise orientation for the U-configuration, as indicated by the larger vertical velocities directly underneath the tailboom.

Forward Flight at an Advance Ratio of 0.35

For the current research effort, the ultimate goal was to achieve drag and download reductions in a range of angles of attack and advance ratios that are representative of a rotorcraft in forward flight. These were determined to be fuselage angles of attack in the range from -3° to -6° at an advance ratio of 0.35 with a rotor thrust coefficient, C_T/σ , of 0.075. At the advance ratio of 0.350, only the steady blowing had the required control authority to reduce the aerodynamic loads acting on the fuselage. Fig. 12 presents the effect of steady blowing on the fuselage drag and lift as a function of angle of attack at a constant level of excitation on a per-slot basis throughout, which results in a $C_\mu = 1.84\%$ for the Ux45 configuration and a $C_\mu = 2.28\%$ for the U configuration. The data presented indicates that steady blowing in the U-configuration reduces the drag uniformly across the angle of attack range tested providing about a 30% reduction for all angles of attack. For steady blowing in the Ux45-configuration, there is an increasing level of drag reduction as the angle of attack becomes more negative. At 0° angle of attack, the Ux45-configuration actually results in a slight increase in drag, but at -6° angle of attack, there is a 25% reduction in drag. The Ux45-configuration does prove more capable of producing a download reduction. As shown in Fig. 12(b), steady blowing in the Ux45-configuration delivered download reductions on the order of 50-60% across the entire range of angles of attack tested with a maximum reduction of 59% occurring at an angle of attack of -2° . Steady blowing in the U-configuration produced a 30% increase in the download at 0° angle of attack. However, once the fuselage reaches -2° angle of attack, the U-configuration is producing download reductions leading to a reduction of 25% at -6° angle of attack. Since the rotor provides both the lifting force for the rotorcraft and the propulsive force for forward flight, determining which reduction is more desirable would depend on other requirements.

Using the same conventions established in the previous section, the PIV results for an advance ratio of 0.350 are considered and presented in Fig. 13. Overall, the features are similar to the features at an advance ratio of 0.25. The baseline velocity field has two low out-of-plane velocity regions

on either side of the tailboom and between them, there is a region of large vertical velocity that is roughly as wide as the tailboom. At this higher advance ratio, the width of the wake is slightly smaller than at a $\mu = 0.25$ and slightly smaller than the width of the fuselage. For the U-configuration, Fig. 13(b), the low out-of-plane velocity region on the port side has been eliminated and the one on the starboard side has been moved away from the tailboom. Again, the vertical velocity in the area directly under the tailboom has been reduced compared to the baseline. The Ux45-configuration, Fig. 13(c), also exhibits a large region of low out-of-plane velocity directly under the tailboom. In Fig. 13(d), it can be seen that this is a region of slightly reversed flow with the recirculation reaching a maximum speed of 18% of the freestream. The width of the wake in the Ux45-configuration closely matches the width of the wake in the baseline, with the wake expanding slightly on the retreating side for the U-configuration.

Forward Flight at an Advance Ratio of 0.225

The highest freestream velocity at which the synthetic jets were able to demonstrate sufficient authority for drag and download reduction corresponds to an advance ratio of 0.225. The performance of the synthetic jet actuation over a range of angles of attacks for primarily the Ux45-configuration is presented in Fig. 14. For this data, the frequency was the same for both configurations, 6/Rev, which corresponds to a $F^+ = 1.28$, and the excitation on a per-slot basis was the same resulting in a $C_\mu = 1.03\%$ for the Ux45-configuration and a $C_\mu = 1.33\%$ for the U-configuration. The synthetic jets were operated so that each jet was 180° out of phase with its neighbor.

The application of control in the Ux45-configuration at zero degrees angle of attack results in an increase in drag. The maximum drag reduction was observed at a fuselage angle of attack of -6° , with the data obtained -3° also showing a decrease in drag. If the trend of the data holds, the Ux45-configuration reduces the drag within the angle of attack range of -1.2° to -6° . There is a download reduction produced by the Ux45-configuration across the entire angle of attack range with the maximum reduction also at a fuselage angle of attack of -6° . The maximum drag and download reduction for the Ux45-configuration was 22% and 43%, respectively. For the U-configuration, maximum drag and download reduction also occur at a fuselage angle of attack of -6° and were 16% and 14%, respectively. For the synthetic jet excitation, the Ux45-configuration performs far better than the U-configuration.

The point for the zero degree angle of attack in Fig 14(b) is included for completeness. The uncertainty associated with that point is very high due to the accuracy of the balance and the fact that the magnitude of the lift force for the baseline is very close to zero and the effect of the control is to reduce the magnitude of the lift force even closer to zero (Refs. 11, 13).

For the PIV acquisition, the synthetic jets introduce the need to look at several different rotor azimuth angles. The drive signals for the synthetic jet actuators were synchronized to the 1/Rev pulse generated by GRMS when the leading edge

of blade 1 passes over the tail. The synthetic jets were operated at a frequency of 6/Rev, which means that as blade 1 sweeps from 0° to 60° , the actuator goes through one complete cycle. PIV image pairs were acquired at three different rotor azimuth angles, 23° , 38° , and 53° and are presented in Fig. 15. The effect of the rotor blade passage on the baseline can be seen in Figs 15(a)-15(c). The unsteadiness of the wake can be seen in the strength and direction of the in-plane velocity directly under the tailboom. The U-configuration reveals itself less capable here with unsteady excitation than it did with steady excitation. There is only a slight reduction in the magnitude of the vertical velocity directly under the tailboom and the regions of low out-of-plane velocity are only slightly altered. The Ux45-configuration, Figs 15(g)-15(i), is successful in maintaining the large region of reversed flow that was seen in the steady cases. Given the performance of the synthetic jet excitation at this advance ratio and the findings presented previously about “building the U,” the synthetic jet concept is still attractive for this application. It will require, however, the development of synthetic jet actuators with higher jet velocities than those utilized here.

Closing Thoughts

The mechanisms through which the drag and download that act upon a rotorcraft fuselage under the influence of a rotor were successfully reduced by utilizing active flow control have been examined. It was shown that the application of flow control, in both the U- and the Ux45-configurations, changes the trajectory of the wake behind the ramp of the ROBIN-mod7 fuselage. It is this altered trajectory of the wake that changes the surface pressure distribution on the ramp, which results in the lower load levels observed.

The flow in the baseline case, while separated, tends to follow the fuselage geometry resulting in a wake that is about the width of the fuselage and dominated by two low streamwise velocity regions underneath and on either side of the tailboom. In between these low-speed regions, there is a region of large vertical velocity that is roughly as wide as the tailboom as would be expected if the flow is primarily following the contour of the ramp. When control is applied, in either the U-configuration or the Ux45-configuration, the result is a wake more aligned with the streamwise direction. The Ux45-configuration produces a large area of reversed flow directly under the tailboom that seems to be directly related to its superior download reduction.

The steady blowing control performed these modifications very well, particularly in the range of angles of attack of interest and at advance ratios that are representative of a rotorcraft in forward flight. Successful application of flow control with the synthetic jet excitation required operating at an advance ratio of 0.225 or less. The observed flow field changes for the synthetic jets operated in the Ux45-configuration are very similar to the steady blowing modifications, with the U-configuration exhibiting more differences between the two control techniques. The requirement to operate at an advance ratio of 0.225 or less in order to have successful synthetic jet

control is directly related to the maximum peak jet velocity that can be developed by the synthetic jets. For the synthetic jet excitation to be applied at higher advance ratios, the development of actuators with higher peak exit velocities would be required.

Acknowledgments

This work was supported by the NASA Rotary Wing Project, now the Revolutionary Vertical Lift Technology Project, and the support of Susan A. Gorton, Project Manager, is gratefully acknowledged. The synthetic jet actuators used in this research effort were designed, fabricated, and installed by Dave Domzalski of Domzalski Machine. This work would not have been possible without the hard work and dedication of the Army/NASA rotorcraft team, past and present, particularly Austin Overmeyer, Bryan Mann, Andy Harrison, Stephen “Fred” Mason, Brendon Malovrh, Preston Martin, Jim Hallisy, Kevin Noonan, and Wayne Mantay. This work would not have been possible without the hard work and dedication of the entire 14x22 staff, particularly the lead test engineer Josh Ballard, Jim Byrd, Ben Trower, Andy Boney and Joe Burton Jr.

References

- ¹Leishman, J. G., *Principles of Helicopter Aerodynamics*, Cambridge University Press, 2nd ed., 2006.
- ²Gatard, J., Costes, M., Kroll, N., Renzoni, P., Kokkalis, A., Rocchetto, A., Serr, C., Larrey, E., Filippone, A., and Wehr, D., “High Reynolds Number Helicopter Fuselage Test in the ONERA F1 Pressureized Wind Tunnel,” 23rd European Rotorcraft Forum Paper 167, Dresden, Germany, September 16-18, 1997.
- ³Martin, P. B., Tung, C., Hassan, A. A., Cerchie, D., and Roth, J., “Active Flow Control Measurements and CFD on a Transport Helicopter Fuselage,” American Helicopter Society 61st Annual Forum, Paper 61, Grapevine, TX, 2005.
- ⁴Ben-Hamou, E., Arad, E., and Seifert, A., “Generic Transport Aft-Body Drag Reduction using Active Flow Control,” AIAA Paper 2004-2509, 2004, [doi:10.2514/6.2004-2509](https://doi.org/10.2514/6.2004-2509).
- ⁵Schaeffler, N. W., Allan, B. G., Lienard, C., and Le Pape, A., “Progress Towards Fuselage Drag Reduction via Active Flow Control: A Combined CFD and Experimental Effort,” 36th European Rotorcraft Forum, Paper 63, Paris, France, 7-9 September 2010, [NTRS Document ID: 2010033120](https://ntrs.nasa.gov/doc/2010033120).
- ⁶Woo, G. T. K., Glezer, A., and Crittenden, T. M., “Transitory Control of Aerodynamic Forces on a ROBIN Fuselage using Pulsed Actuation,” 37th European Rotorcraft Forum, Paper 161, Ticino Park, Italy, 2011.
- ⁷Coleman, D. and Thomas, F. O., “Rotorcraft Fuselage Flow Control Using Plasma Streamwise Vortex Generators,” 65th Annual Meeting of the APS Division of Fluid Dynamics, Volume 57, Number 17, American Physical Society, November 2012.

- ⁸Le Pape, A., Lienard, C., Verbeke, C., Pruvost, M., and De Coninck, J., “Helicopter Fuselage Drag Reduction Using Active Flow Control: a Comprehensive Experimental Investigation,” *Journal of the American Helicopter Society*, Vol. 60, 2015, pp. 032003:1 – 032003:12, doi:10.4050/JAHS.60.032003.
- ⁹Allan, B. G. and Schaeffler, N. W., “Numerical Investigation of Rotorcraft Fuselage Drag Reduction using Active Flow Control,” American Helicopter Society 67th Annual Forum, Paper 111, Virginia Beach, Virginia, 2011, NTRS Document ID: 20110011552.
- ¹⁰Watkins, A. N., Leighty, B. D., Lipford, W. E., Goodman, K. Z., Crafton, J., and Gregory, J. W., “Applying Pressure Sensitive Paint Technology to Rotor Blades,” NASA TM 2014-218259, Langley Research Center, 2014, NTRS Document ID: 20140006409.
- ¹¹Schaeffler, N. W., Allan, B. G., Wong, O. D., and Tanner, P. E., “Experimental Investigation of Active Aerodynamic Load Reduction on a Rotorcraft Fuselage with Rotor Effects,” AIAA Paper 2014-2561, 2014, doi:10.2514/6.2014-2561.
- ¹²Martin, P. B., Overmeyer, A. D., Tanner, P. E., Wilson, J. S., and Jenkins, L. N., “Helicopter Fuselage Active Flow Control in the Presence of a Rotor,” American Helicopter Society 70th Annual Forum, Paper 335, Montréal, Québec, Canada, 2014.
- ¹³Ballard, J. G., Overmeyer, A. D., Schaeffler, N. W., Allan, B. G., Jenkins, L. N., Martin, P. B., Tanner, P. E., Wong, O. D., and Mace, W. D., “Joint Army/NASA Rotorcraft Active Flow Control Testing at the NASA Langley Research Center 14- by 22-Foot Subsonic Tunnel,” NASA TM In Preparation, Langley Research Center, 2016.
- ¹⁴Gentry, G. L., Quinto, P. F., Gatlin, G. M., and Applin, Z. T., “The Langley 14- by 22-Foot Subsonic Tunnel: Description, Flow Characteristics and Guide for Users,” NASA TP- 3008, NASA Langley Research Center, 1990.
- ¹⁵Wong, O. D., Watkins, A. N., Goodman, K. Z., Crafton, J., Forlines, A., Goss, L., Gregory, J. W., and Juliano, T. J., “Blade Tip Pressure Measurements Using Pressure Sensitive Paint,” American Helicopter Society 68th Annual Forum, Paper 233, Fort Worth, TX, 2012.
- ¹⁶Wilson, J. C., “A General Rotor Model System for Wind-Tunnel Investigations,” *Journal of Aircraft*, Vol. 14, (7), July 1977, pp. 639–643, doi:10.2514/3.58834.
- ¹⁷Freeman, C. and Mineck, R. E., “Fuselage Surface Pressure Measurements of a Helicopter Wind-Tunnel Model with a 3.15-meter Diameter Single Rotor,” NASA TM 80051, Langley Research Center, March 1979, NTRS Document ID: 19790017844.
- ¹⁸Phelps, A. E. and Berry, J. D., “Description of the U. S. Army Small-Scale 2-Meter Rotor Test System,” NASA TM 87762 (AVSCOM TM-86-B-4), Langley Research Center, February 1987, NTRS Document ID: 19870008231.
- ¹⁹Mineck, R. and Gorton, S. A., “Steady and Periodic Pressure Measurements on a Generic Helicopter Fuselage Model in the Presence of a Rotor,” NASA TM 2000-210286, Langley Research Center, June 2000, NTRS Document ID: 20000057579.
- ²⁰Renaud, T., O’Brien, D., Smith, M., and Potsdam, M., “Evaluation of Isolated Fuselage and Rotor-Fuselage Interaction Using CFD,” American Helicopter Society 60th Annual Forum, Baltimore, Maryland, June 2004.
- ²¹O’Brien, D. M. and Smith, M. J., “Analysis of Rotor-Fuselage Interactions Using Various Rotor Models,” AIAA Paper 2005-0468, January 2005, doi:10.2514/6.2005-468.
- ²²Kunze, P., “Parametric Fuselage Geometry Generation and Aerodynamic Performance Prediction in Preliminary Rotorcraft Design,” 39th European Rotorcraft Forum, Paper 122, Moscow, Russia, 3-6 September 2013.
- ²³Abras, J. N. and Hariharan, N., “CFD Solver Comparison of Low Mach Flow over the ROBIN Fuselage,” AIAA Paper 2014-0752, 2014, doi:10.2514/6.2014-0752.
- ²⁴Shenoy, R., Holmes, M., Smith, M. J., and Komerath, N. M., “Scaling Evaluations on the Drag of a Hub System,” *Journal of the American Helicopter Society*, Vol. 58, (3), July 2013, pp. 032002.1–032002.13, doi:10.4050/JAHS.58.032002.
- ²⁵Kim, J. W., Sankar, L., Min, B. Y., Yeshala, N., and Egolf, T. A., “Multiscale Modeling of Active Flow Control for Fuselage Drag Reduction,” AIAA Paper 2012-0075, January 2012, doi:10.2514/6.2012-75.
- ²⁶Spalart, P. and Allmaras, S. R., “One-Equation Turbulence Model for Aerodynamic Flows,” AIAA Paper 1992-0439, 1992, doi:10.2514/6.1992-439.
- ²⁷Menter, R. F., “Two-Equation Eddy-Viscosity Turbulence Models for Engineering Applications,” *AIAA Journal*, Vol. 32, (8), 1994, pp. 1598–1605, doi:10.2514/3.12149.
- ²⁸Shur, M., Strelets, M., Travin, A., and Spalart, P., “Turbulence Modeling in Rotating and Curved Channels: Assessing the Spalart-Shur Correction,” *AIAA Journal*, Vol. 38, (5), May 2000, pp. 784–792, doi:10.2514/2.1058.
- ²⁹Johnson, W., “Rotorcraft Aerodynamics Models for a Comprehensive Analysis,” American Helicopter Society 54th Annual Forum Proceedings, Washington, D.C., May 20-22, 1998.
- ³⁰Johnson, W., “CAMRAD II Comprehensive Analytical Model of Rotorcraft Aerodynamics and Dynamics,” Johnson Aeronautics, Palo Alto, California, 2005.
- ³¹Allan, B. G., Schaeffler, N. W., Jenkins, L. N., Yao, C. S., Wong, O. D., and Tanner, P. E., “Active Aerodynamic Load Reduction on a Rotorcraft Fuselage with Rotor Effects - A CFD Validation Effort,” American Helicopter Society 71th Annual Forum, Paper 219, Virginia Beach, Virginia, 2015.

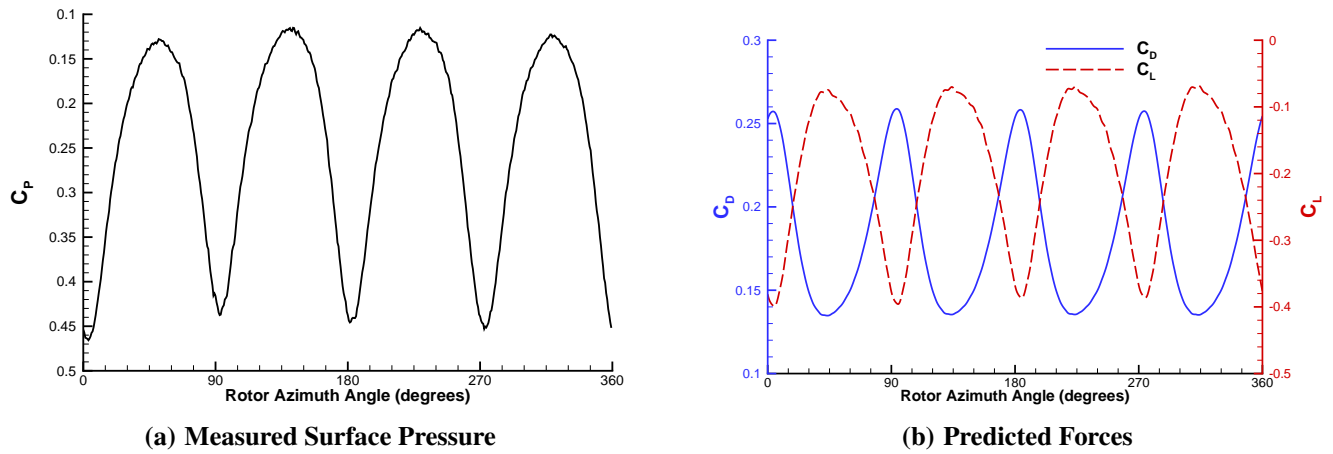


Fig. 5. Measured surface pressure from the upper section of the nose of the fuselage and the predicted aerodynamic loads from OVERFLOW as a function of rotor azimuth angle at $\mu = 0.250$, $C_T/\sigma = 0.075$, and $\alpha = -6^\circ$.

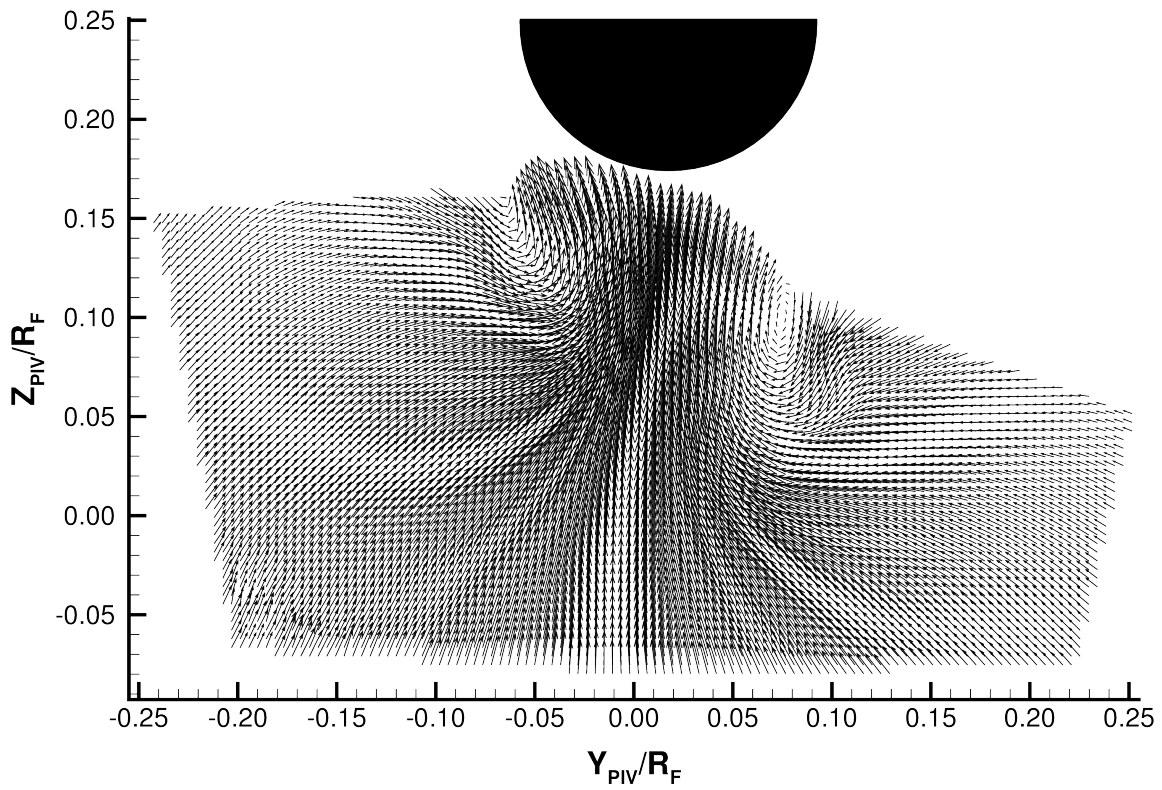


Fig. 6. A representative complete measured velocity field. The vectors are comprised of the in-plane velocity components. The black semi-circle represents the size and location of the tailboom, relative to the measurement plane.

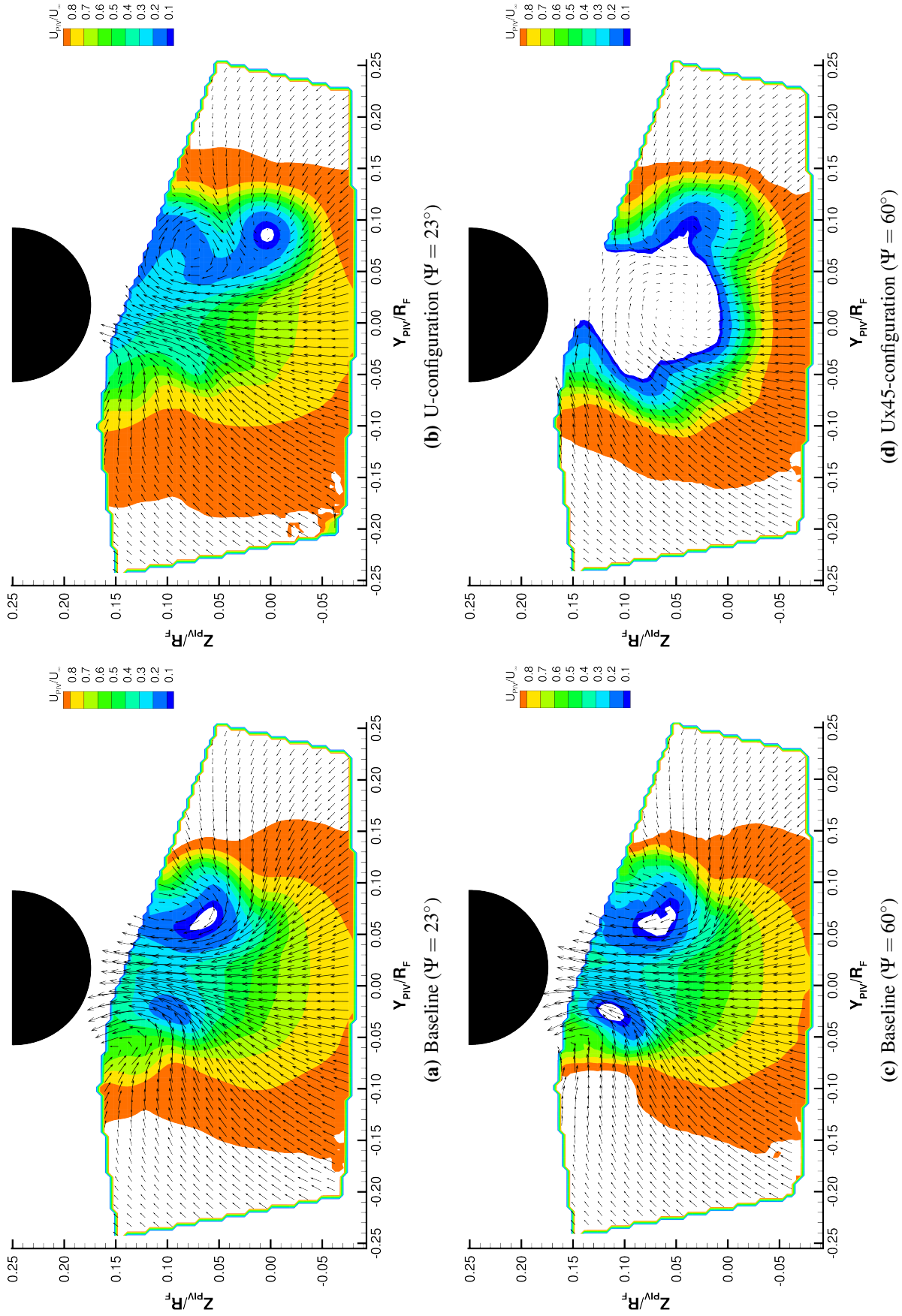


Fig. 7. Measured velocity fields for the Baseline and U-configuration at a rotor azimuth angle of 23° and the Baseline and Ux45-configuration at a rotor azimuth angle of 60° . AFC = Steady blowing at $C_\mu = 2.07\%$ for the U-configuration and $C_\mu = 1.67\%$ for the Ux45-configuration, $\mu = 0.250$, $C_T/\sigma = 0.075$, and $\alpha = -6^\circ$.

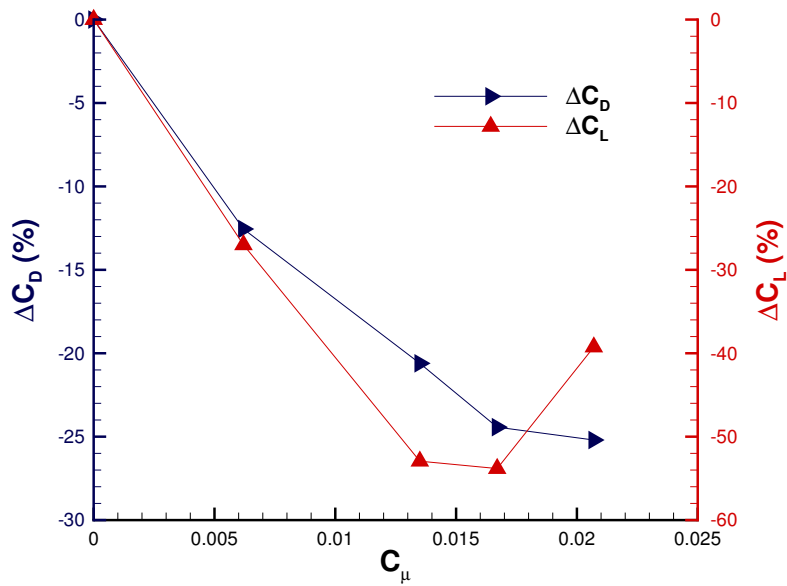


Fig. 8. Change in drag and lift coefficients as a function of the momentum coefficient, C_μ . Each C_μ value represents an additional pair of slots becoming active, in sequence starting with the upper pair, slots 1 and 8. AFC = Steady blowing, $\mu = 0.250$, $C_T/\sigma = 0.075$, and $\alpha = -6^\circ$.

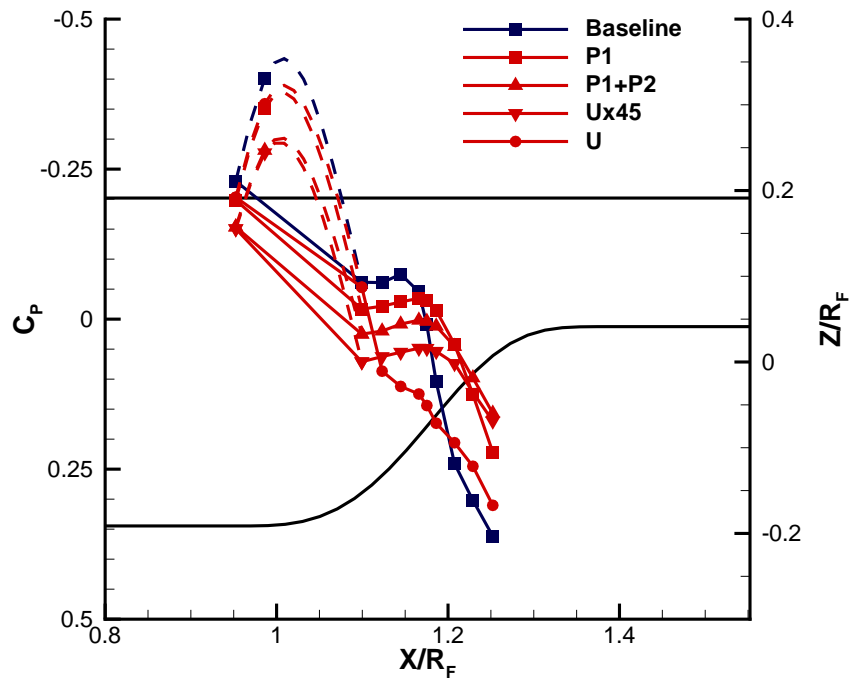


Fig. 9. Surface pressure distribution over the fuselage ramp section for several steady blowing configurations at $\mu = 0.250$, $C_T/\sigma = 0.075$, and $\alpha = -6^\circ$.

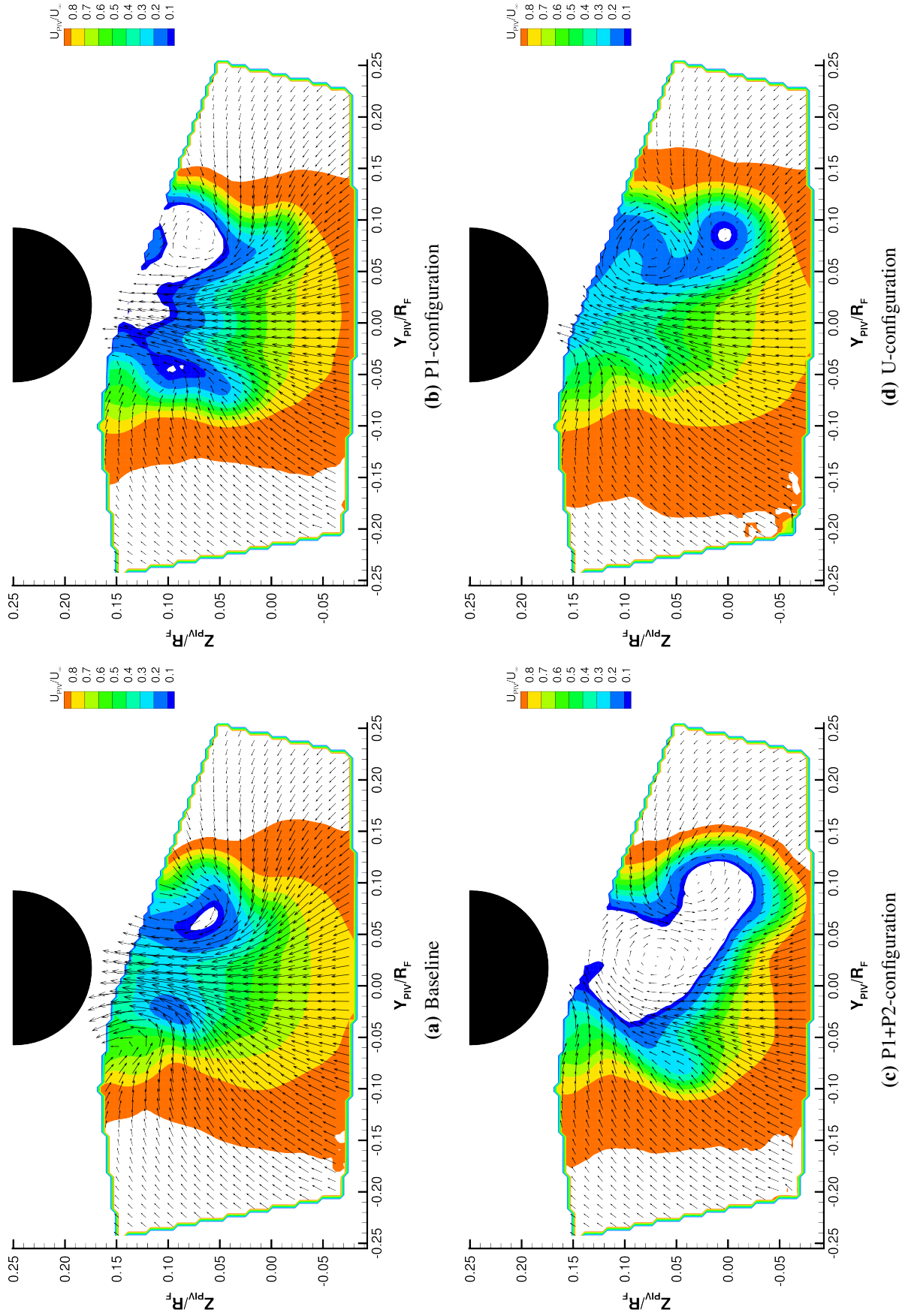


Fig. 10. Measured velocity fields for the Baseline and the steady blowing configurations, P1, P1+P2, and U, at the rotor azimuth angles of 23° . $\mu = 0.250$, $C_T/\sigma = 0.075$, and $\alpha = -6^\circ$.

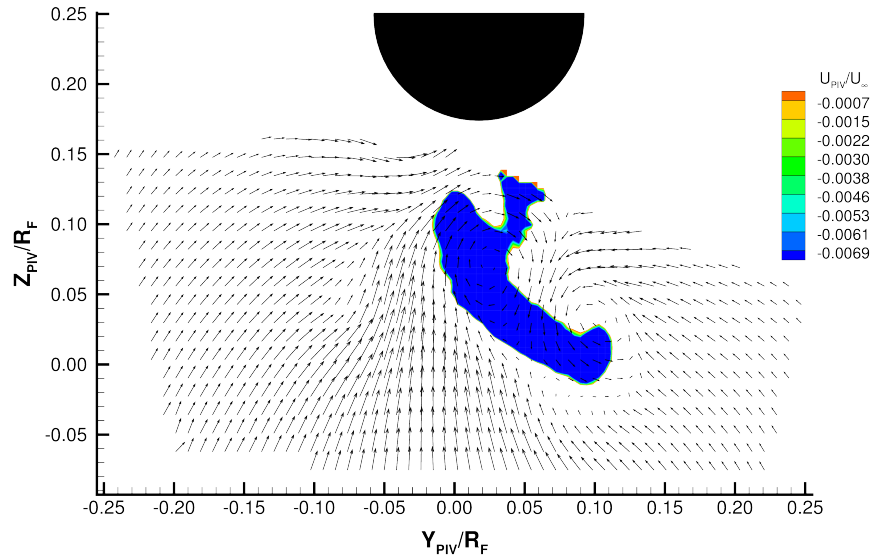


Fig. 11. Measured velocity field for the steady blowing P1+P2-configuration (Slots 1-2 and 7-8 active) with reverse flow contours at $\Psi = 23^\circ$, $C_\mu = 0.014$, $\mu = 0.250$, $C_T/\sigma = 0.075$, $\alpha = -6^\circ$.

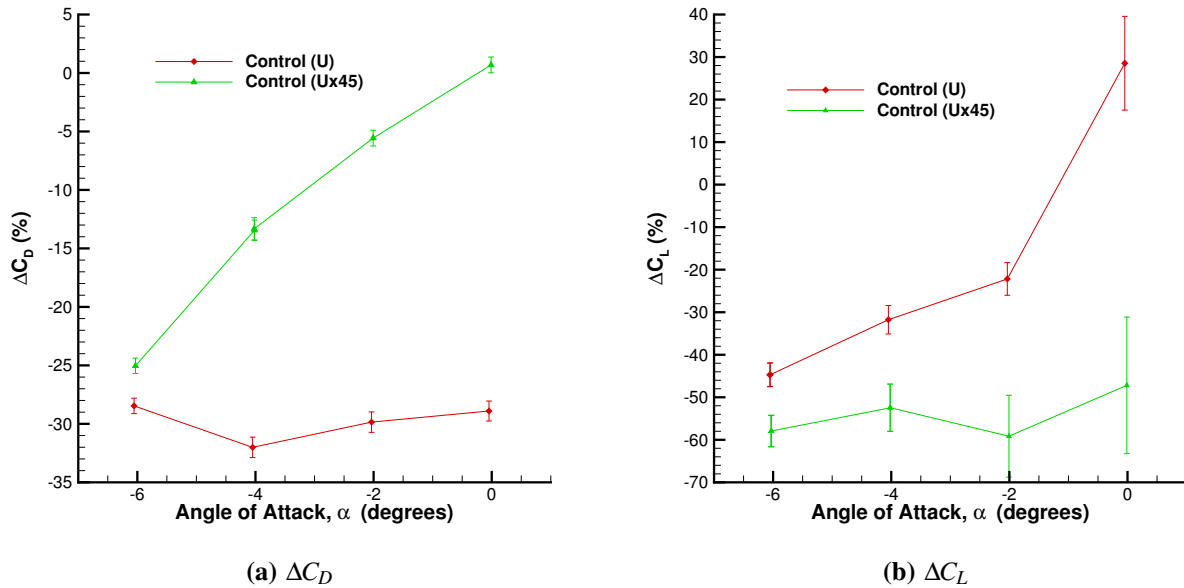


Fig. 12. Effect of steady blowing on the fuselage drag and lift as a function of angle of attack. The level of excitation on a per-slot basis was the same throughout resulting in a $C_\mu = 1.84\%$ for the Ux45-configuration and a $C_\mu = 2.28\%$ for the U-configuration. Rotor conditions were $\mu = 0.350$ and $C_T/\sigma = 0.075$.

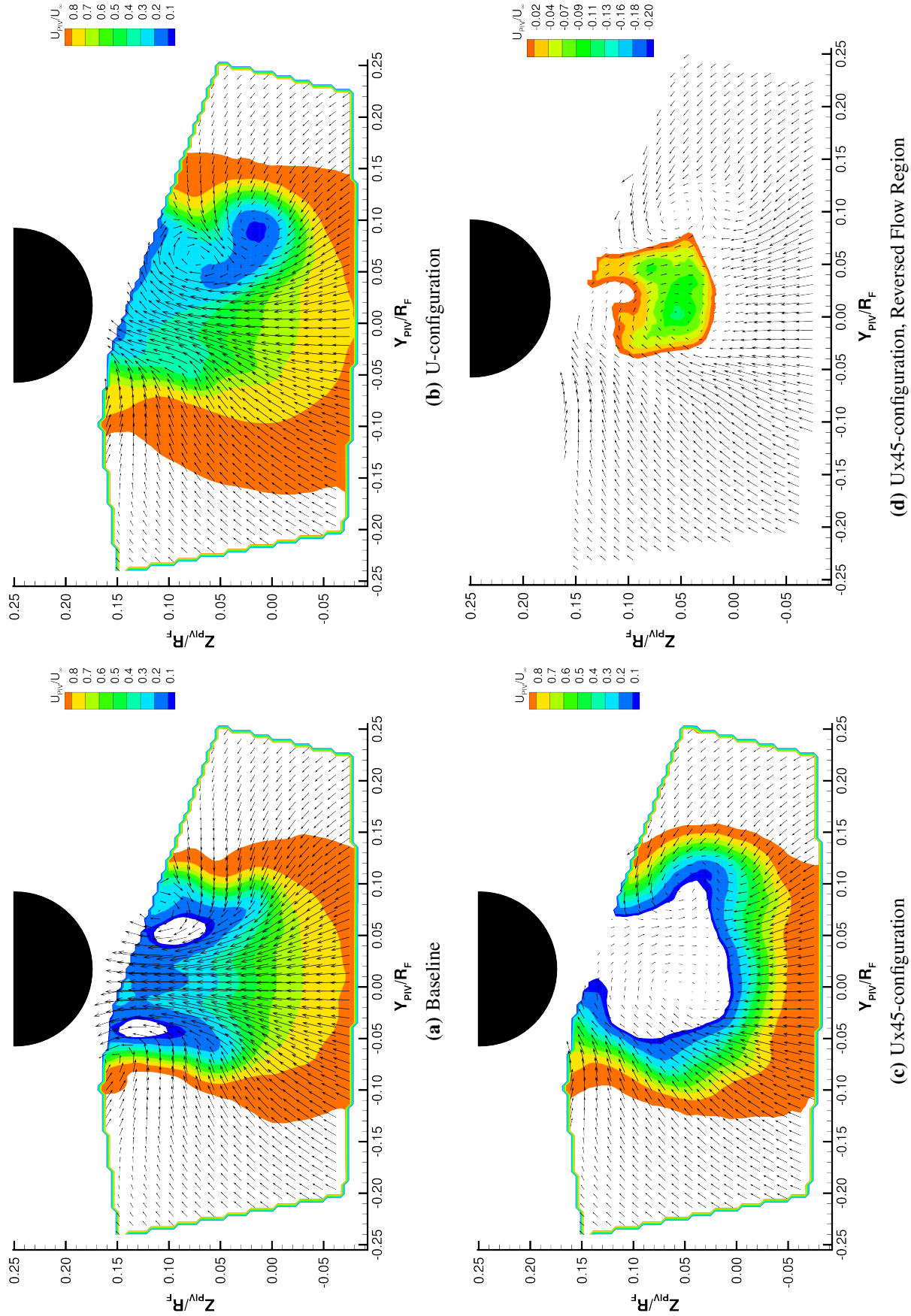
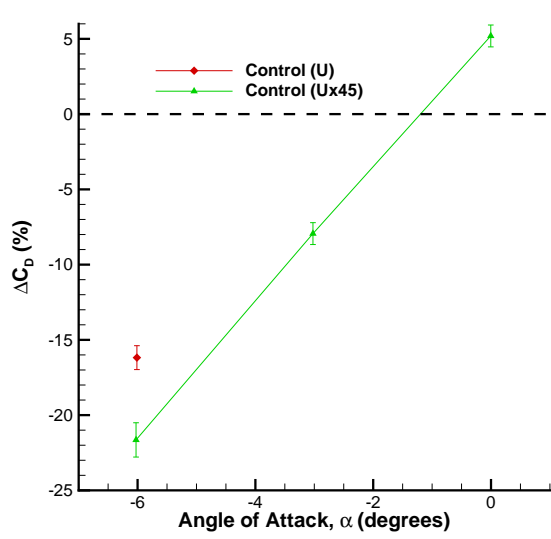
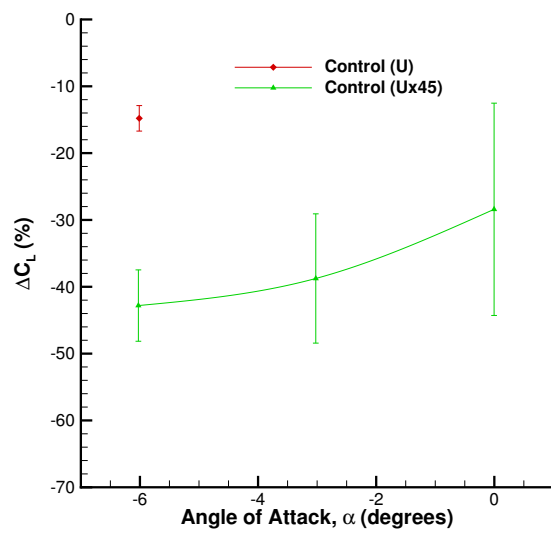


Fig. 13. Measured velocity fields for the Baseline, U-configuration, and Ux45-configuration of steady blowing at $\Psi = 23^\circ$. AFC = Steady blowing at $C_\mu = 1.84\%$ for the Ux45-configuration and $C_\mu = 2.28\%$ for the U-configuration, $\mu = 0.350$, $C_T/\sigma = 0.075$, $C_T/\sigma = 0.075$, $\alpha = -6^\circ$.



(a) ΔC_D



(b) ΔC_L

Fig. 14. Effect of synthetic jet control on the fuselage drag and lift as a function of angle of attack. The synthetic jets were operated at the same frequency, $F^+ = 1.28(6/Rev)$, and excitation level throughout. This results in a $C_{\mu} = 1.03\%$ for the Ux45-configuration and $C_{\mu} = 1.33\%$ for the U-configuration. Rotor conditions were $\mu = 0.225$ and $C_T/\sigma = 0.075$.

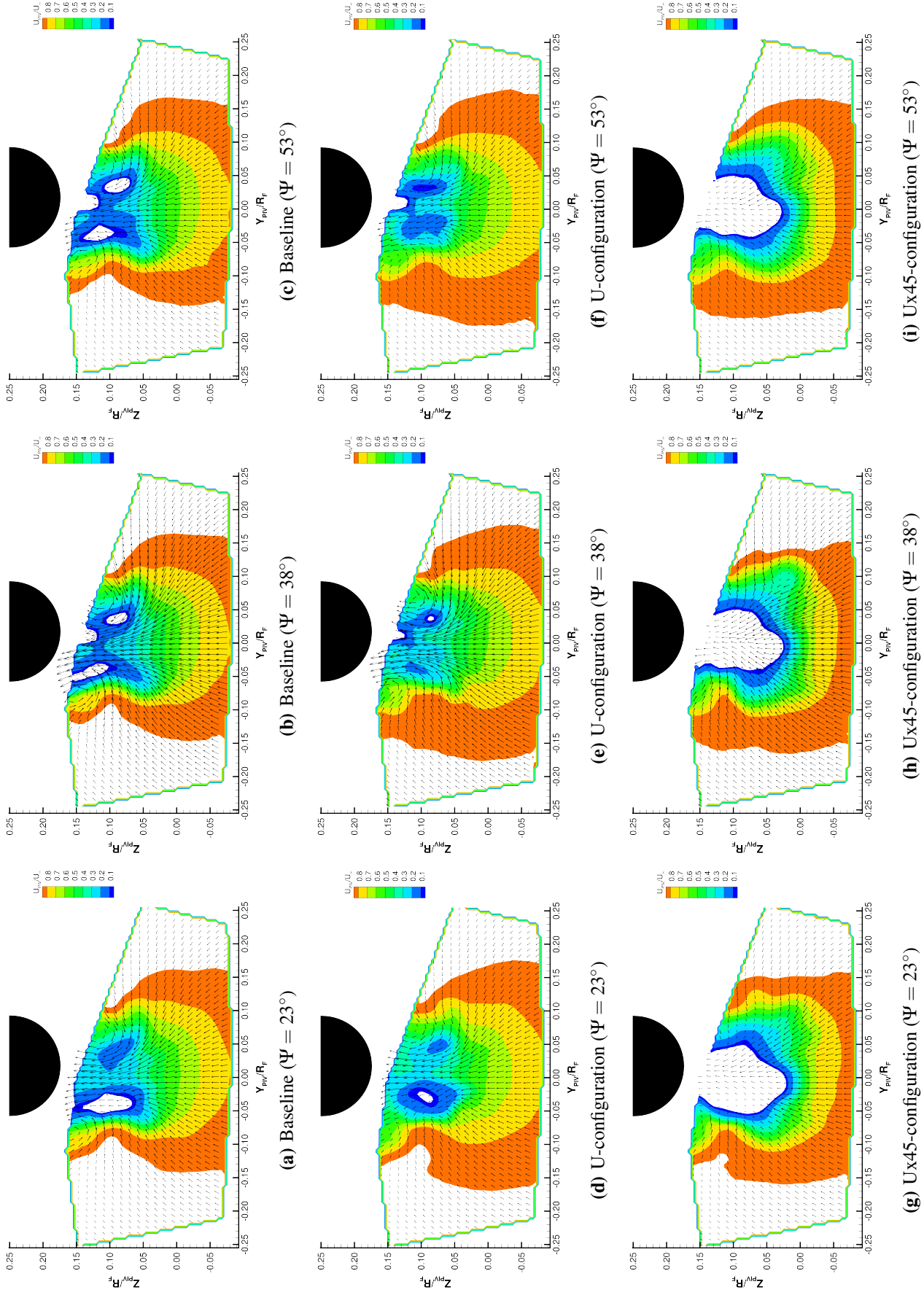


Fig. 15. Measured velocity fields for the Baseline, U-, and Ux45-configurations at the rotor azimuth angles of 23° , 38° , and 53° . AFC = Synthetic jets, $\mu = 0.225$, $C_T/\sigma = 0.075$, and $\alpha = -6^\circ$.